nature communications

Article

https://doi.org/10.1038/s41467-025-55889-9

Ammonia electrosynthesis from nitrate using a stable amorphous/crystalline dual-phase Cu catalyst

Received: 15 May 2024

Accepted: 3 January 2025

Published online: 21 January 2025

Check for updates

Yi Wang[1,2,3], Shuo Wang[1,3], Yunfan Fu[1,2], Jiaqi Sang[1,2], Pengfei Wei[1], Rongtan Li[1], Dunfeng Gao[1] ✉, Guoxiong Wang[1] ✉ & Xinhe Bao[1]

Renewable energy-driven electrocatalytic nitrate reduction reaction presents a low-carbon and sustainable route for ammonia synthesis under mild conditions. Yet, the practical application of this process is currently hindered by unsatisfactory electrocatalytic activity and long-term stability. Herein we achieve high-rate ammonia electrosynthesis using a stable amorphous/crystalline dual-phase Cu catalyst. The ammonia partial current density and formation rate reach 3.33 ± 0.005 A cm^{-2} and 15.5 ± 0.02 mmol h^{-1} cm^{-2} at a low cell voltage of 2.6 ± 0.01 V, respectively. Remarkably, the dual-phase Cu catalyst can maintain stable ammonia production with a Faradaic efficiency of around 90% at a high current density of 1.5 A cm^{-2} for up to 300 h. A scale-up demonstration with an electrode size of 100 cm^2 achieves an ammonia formation rate as high as 11.9 ± 0.5 g h^{-1} at a total current of 160 A. The impressive electrocatalytic performance is ascribed to the presence of stable amorphous Cu domains which promote the adsorption and hydrogenation of nitrogen-containing intermediates, thus improving reaction kinetics for ammonia formation. This work underscores the importance of stabilizing metastable amorphous structures for improving electrocatalytic reactivity and long-term stability.

Ammonia (NH_3) is currently produced by the energy-intensive Haber–Bosch process which converts nitrogen (N_2) and hydrogen (H_2) to NH_3 at high temperatures (400–500 °C) and high pressures (10–30 MPa). The Haber–Bosch process accounts for 1–2% of global energy consumption and roughly 1% of global CO_2 emission[1,2]. Alternative routes for green NH_3 synthesis under mild conditions are highly desired. The renewable energy-driven electrocatalytic nitrate reduction reaction (NO_3^-RR), with NO_3^- (with concentrations from hundreds of ppm to >1 M) from wastewater being as a nitrogen source and water being as a hydrogen source, provides a low-carbon route for green NH_3 synthesis under ambient conditions, with promising energy and environmental sustainability[3,4].

The NH_3 production via NO_3^-RR involves multiple proton and electron transfer steps ($NO_3^- + 6H_2O + 8e^- \rightarrow NH_3 + 9OH^-$), leading to sluggish reaction kinetics[5]. The NO_3^-RR rate is governed by the adsorption of nitrogen species present during NO_3^-RR and the formation of active hydrogen species from water dissociation[6,7]. An efficient catalyst for NO_3^-RR should exhibit balanced adsorption of the above intermediates, thus directing the reaction pathway to NH_3 at a high reaction rate while minimizing the formation of side products such as nitrite (NO_2^-) and H_2[8,9]. The adsorption of these intermediates is highly dependent on the geometric and electronic structures of metal catalysts, as demonstrated by remarkably distinct NO_3^-RR performances over noble metal (e.g., Pt, Ru, Pd)[6,10,11], non-noble metal (e.g., Fe, Co, Ni, Cu)[7,12–18], and bimetallic (e.g., CuPd, CuNi) catalysts[19–23]. Cu has been recognized as one of the most active non-noble metals, owing to its prominent ability for the conversion of NO_3^- to NO_2^-[4,24]. To date, while Cu-based catalysts have exhibited high NH_3 Faradaic

[1]State Key Laboratory of Catalysis, Dalian National Laboratory for Clean Energy, iChEM (Collaborative Innovation Center of Chemistry for Energy Materials), Dalian Institute of Chemical Physics, Chinese Academy of Sciences, Dalian, China. [2]University of Chinese Academy of Sciences, Beijing, China. [3]These authors contributed equally: Yi Wang, Shuo Wang. ✉e-mail: dfgao@dicp.ac.cn; wanggx@dicp.ac.cn

efficiency[25], their activity and stability are still unsatisfactory for practical application.

Amorphous catalytic materials, with extremely disordered atomic arrangement in long range, possess high density of low-coordinated sites which are essential for the adsorption and activation of reactants and intermediates[26,27]. However, the amorphous materials are metastable and prone to suffering from crystallization during reaction, especially under highly reducing electrochemical conditions[28–30]. Here we report a stable amorphous/crystalline dual-phase Cu (a/c-Cu) catalyst for high-rate NH_3 electrosynthesis via NO_3^-RR. The a/c-Cu catalyst exhibits a NH_3 partial current density of 3.33 ± 0.005 A cm^{-2} and a NH_3 formation rate of 15.5 ± 0.02 mmol h^{-1} cm^{-2} at a low cell voltage of 2.6 ± 0.01 V in an alkaline membrane electrode assembly (MEA) electrolyzer. Remarkably, the NH_3 Faradaic efficiency maintains around 90% at an applied current density of 1.5 A cm^{-2} for 300 h. The impressive NO_3^-RR performance is rationalized by the presence of stable amorphous Cu domains which promote NH_3 generation by optimizing the adsorption of N-containing intermediates and facilitating the formation of active hydrogen species from water dissociation.

Results

NO_3^-RR performance of a/c-Cu catalyst

The a/c-Cu catalyst was prepared by annealing a commercially available Cu foam in air at 600 °C followed by in situ electrochemical reduction during NO_3^-RR (Supplementary Fig. 1). The NO_3^-RR performance of the a/c-Cu catalyst was measured in a home-made alkaline MEA electrolyzer (Supplementary Fig. 2). The anolyte and catholyte were 1 M KOH and 1 M KOH + 0.2 M KNO_3 solutions, respectively. The NO_3^-RR measurements were performed in the galvanostatic mode. The gas product (H_2) and liquid products (NH_3 and NO_2^-) were analyzed and quantified using an on-line gas chromatography and an ultraviolet−visible (UV−Vis) spectrophotometer, respectively (Supplementary Figs. 3–5). The quantification of NH_3 was further validated by proton nuclear magnetic resonance (^{1}H NMR) analysis (Supplementary Figs. 6–8). Herein, the annealed Cu foam is directly used as a working electrode. Such an integrated electrode is featured with facile preparation and shows significantly improved electrocatalytic performance compared to a conventional electrode with drop-casted catalyst powder (Supplementary Fig. 9). The three-dimensional and highly porous foam structure can remarkably facilitate mass transport especially at high current densities[31,32]. Figure 1a shows the Faradaic efficiencies and cell voltage as a function of applied current density over the a/c-Cu electrode. The a/c-Cu electrode achieves a peak NH_3 Faradaic efficiency of 92 ± 0.87% at an applied current density of 1.5 A cm^{-2}. The NH_3 Faradaic efficiency still maintains over 83% at an applied current density up to 4.0 A cm^{-2}, which translates into a NH_3 partial current density of 3.33 ± 0.005 A cm^{-2} and a NH_3 formation rate of 15.5 ± 0.02 mmol h^{-1} cm^{-2} at a low cell voltage of 2.6 ± 0.01 V (Supplementary Fig. 10). The effect of annealing temperature on the NO_3^-RR performance was also investigated by further measuring another two Cu foam samples annealed in air at 300 and 900 °C, respectively. The sample annealed at 600 °C (i.e., the a/c-Cu sample) shows the highest NO_3^-RR performance (Supplementary Fig. 11). The NH_3 partial current density over our a/c-Cu electrode measured in 0.2 M KNO_3 outperforms a raw Cu foam electrode (Supplementary Fig. 12) as well as previously reported values achieved even with a higher KNO_3 concentration up to 1 M (Fig. 1b and Supplementary Table 1)[6–8,12,17–20]. The peak full-cell energy efficiency for NH_3 production reaches 26 ± 1% at 1.0 A cm^{-2} and outperforms most of previous studies (Fig. 1c, Supplementary Fig. 9 and Table 2)[14,23,33–35]. The stability test of the a/c-Cu electrode was performed at an applied current density of 1.5 A cm^{-2}. In a course of 300 h, the cell voltage is almost stable and the NH_3 Faradaic efficiency maintains around 90% (Fig. 1d, Supplementary Fig. 13). We tried to scale up the NO_3^-RR process by increasing the geometric electrode area from 1 to 100 cm^2 (Supplementary Fig. 14). As shown in Fig. 1e, the NH_3 Faradaic efficiency reaches 94 ± 3.9% at an applied current of 160 A (the used direct current power supply has an upper current limit of 170 A) and a cell voltage of 2.23 ± 0.005 V. The highest NH_3 formation rate reaches up to 11.9 ± 0.5 g h^{-1} (Supplementary Fig. 15a) and the corresponding energy consumption for NH_3 production is as low as 108.3 ± 0.47 kJ g^{-1}_{NH3} at 160 A (Supplementary Fig. 15b). The reported NO_3^-RR performance in terms of NH_3 formation rate and energy consumption is superior to state-of-the-art cases in the literature (Fig. 1f)[33–36]. Overall, by turning a commercially available Cu foam into an active a/c-Cu catalyst through facile annealing treatment, we have achieved very promising selectivity, reaction rate, and stability towards industrial ammonia synthesis via NO_3^-RR.

Structure characterizations

To reveal structure-reactivity correlations of the a/c-Cu catalyst for the impressive NO_3^-RR performance, a series of structural characterizations and control experiments were conducted. The annealed Cu foam in air at 600 °C was firstly characterized by X-ray diffraction (XRD) and scanning electron microscopy (SEM). The characteristic XRD pattern of a pure CuO phase indicates that the presence of a thick CuO layer on the raw Cu foam after annealing treatment in air (Supplementary Fig. 16). Meanwhile, the original flat surface of the raw Cu foam becomes very rough with irregularly shaped grains (Supplementary Fig. 17). After NO_3^-RR, these large grains disappear and form a rough and porous layer (Supplementary Fig. 18), along with the reduction of CuO revealed by the XRD pattern of the post-reaction sample (Fig. 2a). The *operando* Cu K-edge X-ray absorption near edge structure (XANES) spectra of the a/c-Cu catalyst further confirm that CuO is fully reduced to metallic Cu during NO_3^-RR (Fig. 2b and Supplementary Fig. 19). This is consistent with the results obtained from the Cu LMM Auger spectrum of the *quasi* in situ X-ray photoelectron spectroscopy (XPS) analysis (Supplementary Fig. 20)[37]. The Fourier transformation of the extended X-ray absorption fine-structure (EXAFS) spectra show decreased peak intensity of the Cu-Cu coordination at 2.3 Å (Fig. 2c), and the average Cu coordination number estimated by fitting results is around 6.7 ± 0.4 (Supplementary Figs. 21, 22 and Supplementary Table 3). These results indicate the presence of abundant low-coordinated Cu sites that are in situ generated during NO_3^-RR (Supplementary Fig. 23)[38,39]. High-resolution transmission electron microscopy (HRTEM) images show that the a/c-Cu catalyst consists of abundant amorphous domains which are separated by crystalline regions (Fig. 2d and Supplementary Fig. 24). The amorphous/crystalline dual-phase structure is further confirmed by the corresponding fast Fourier transform (FFT) patterns acquired from amorphous and crystalline regions (Fig. 2e). High-angle annular dark-field scanning transmission electron microscopy (HAADF-STEM) images and energy-dispersive X-ray spectroscopy (EDS) elemental mapping analysis of the a/c Cu catalyst clearly show the co-existence of disordered Cu domains and crystalline Cu domains (Fig. 2f and Supplementary Fig. 25).

To reveal whether the impressive NO_3^-RR performance correlates with the presence of amorphous domains, we further treated the Cu foam annealed in air at 600 °C by annealing in H_2 at 350 °C prior to NO_3^-RR and the control sample was denoted as a/c-Cu-H_2 (Supplementary Figs. 17c and 18c). As indicated by the much sharper XRD characteristic Cu patterns in Fig. 2a, the H_2 annealing treatment results in a significant increase in the crystallinity of the a/c-Cu-H_2 catalyst, compared with the a/c-Cu catalyst. Accordingly, HRTEM images of the a/c-Cu-H_2 catalyst indicate that the amorphous domains reduce drastically (Supplementary Fig. 26). Quantitative and statistical analysis based on ten typical HRTEM images for each sample demonstrates that the ratio of the amorphous domains decreases from 24.1 ± 3.3% over a/c-Cu to 5.5 ± 2.7% over a/c-Cu-H_2 (Fig. 2g). The increased crystallinity (thus, decreased amorphization)

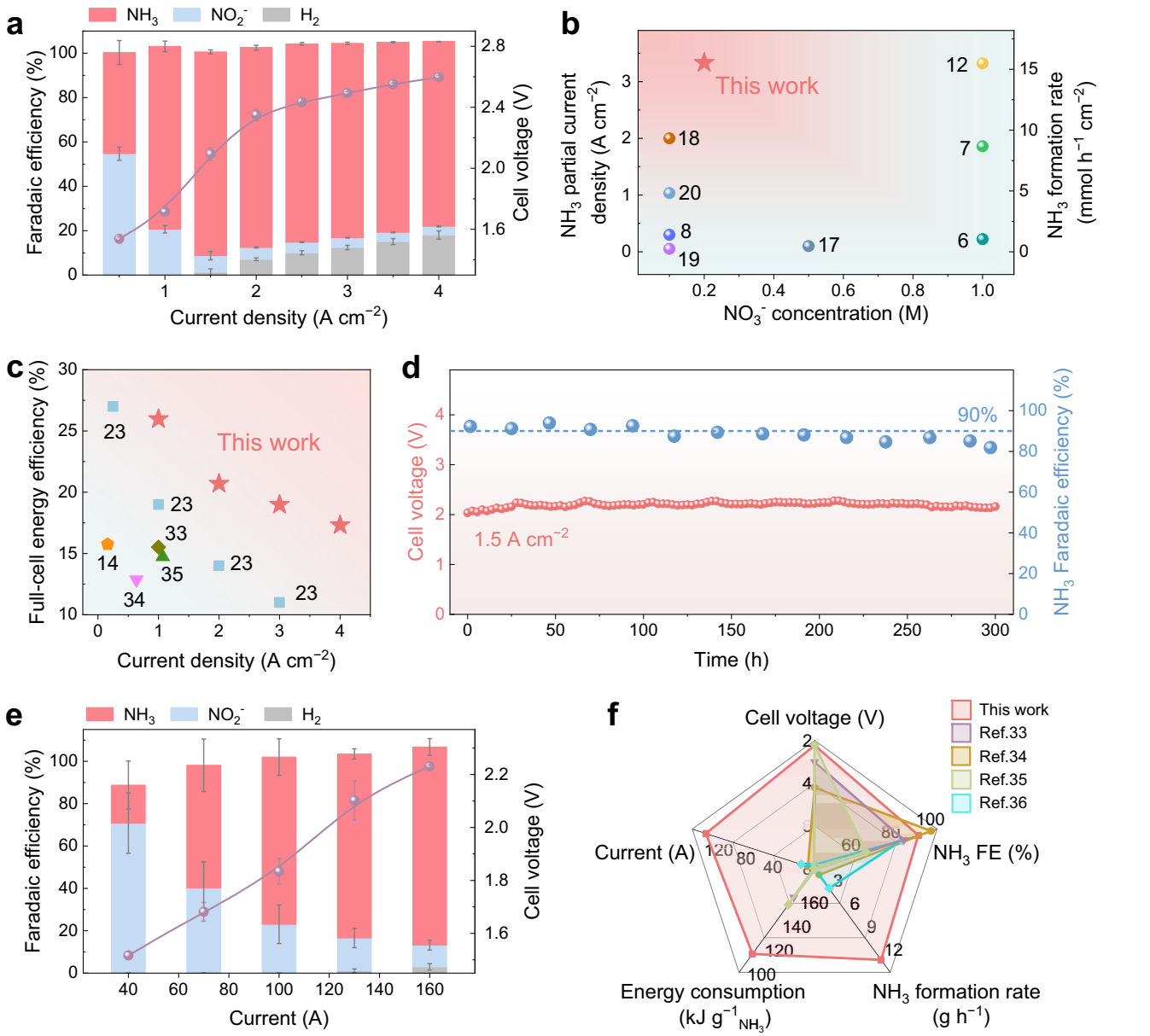

Fig. 1 | NO_3^-RR performance of a/c-Cu catalyst measured in MEA electrolyzers. **a** Faradaic efficiencies and cell voltage as a function of applied current density. Comparisons of **b** performance and **c** full-cell energy efficiency reported in this work measured in a 1-cm^2 electrolyzer with literature[6–8,12,14,17–20,23,33–35]. **d** Stability test at 1.5 A cm^{-2}. **e** Scale-up performance with a 100-cm^2 electrolyzer and **f** performance comparison with literature[33–36]. The error bars represent standard error of the mean and are made based on three fully separate and identical measurements. Source data are provided as a Source Data file.

induced by the H_2 annealing treatment is further evidenced by differential scanning calorimetry (DSC) measurements (Fig. 2h). The exothermic peak observed at around 133 °C is assigned to the crystallization of the amorphous Cu domains[40]. The larger exothermic peak suggests a higher ratio of the amorphous Cu domains in the a/c-Cu catalyst. It is widely accepted that amorphous materials possess abundant low-coordinated sites owing to their long-range atomic disorder[26]. The Pb underpotential deposition (Pb-UPD) was used to characterize the surfaces of the a/c-Cu and a/c-Cu-H_2 catalysts. For the a/c-Cu catalyst, the Pb stripping peak at −0.15 V vs. Ag/AgCl which is assigned to low-coordinated sites is more prominent (Fig. 2i)[41], consistent with its higher ratio of the amorphous domains (Fig. 2g). The NO_3^-RR performance of the a/c-Cu-H_2 catalyst was also measured under identical reaction conditions (Supplementary Fig. 27). As shown in Fig. 2j, the NH_3 current density over the a/c-Cu-H_2 catalyst is much lower than that over the a/c-Cu catalyst at a cell voltage of 2.35 V. These control experiments indicate that the improved ammonia synthesis is positively correlated with the amorphous Cu domains.

It has been reported that amorphous materials are prone to suffering from atomic rearrangement processes such as crystallization under electrochemical reaction conditions[29,42]. We further conducted Pb-UPD measurements over the a/c-Cu catalyst after different reaction durations (0.5, 1.0, and 2.0 h). As shown in Supplementary Figs. 28 and 29, the ratios of main facets and the amounts of low-coordinated sites (thus, amorphous domains) are almost constant over time, indicative of good structural stability of the dual-phase a/c-Cu catalyst during NO_3^-RR. In contrast, a pure amorphous Cu catalyst (a-Cu) quickly turns crystalline under NO_3^-RR conditions (Supplementary Fig. 30). Therefore, it is speculated that the amorphous Cu domains in the a/c Cu catalyst are likely kinetically stabilized by adjacent crystalline Cu domains[43,44]. The a/c-Cu catalyst after reaction at

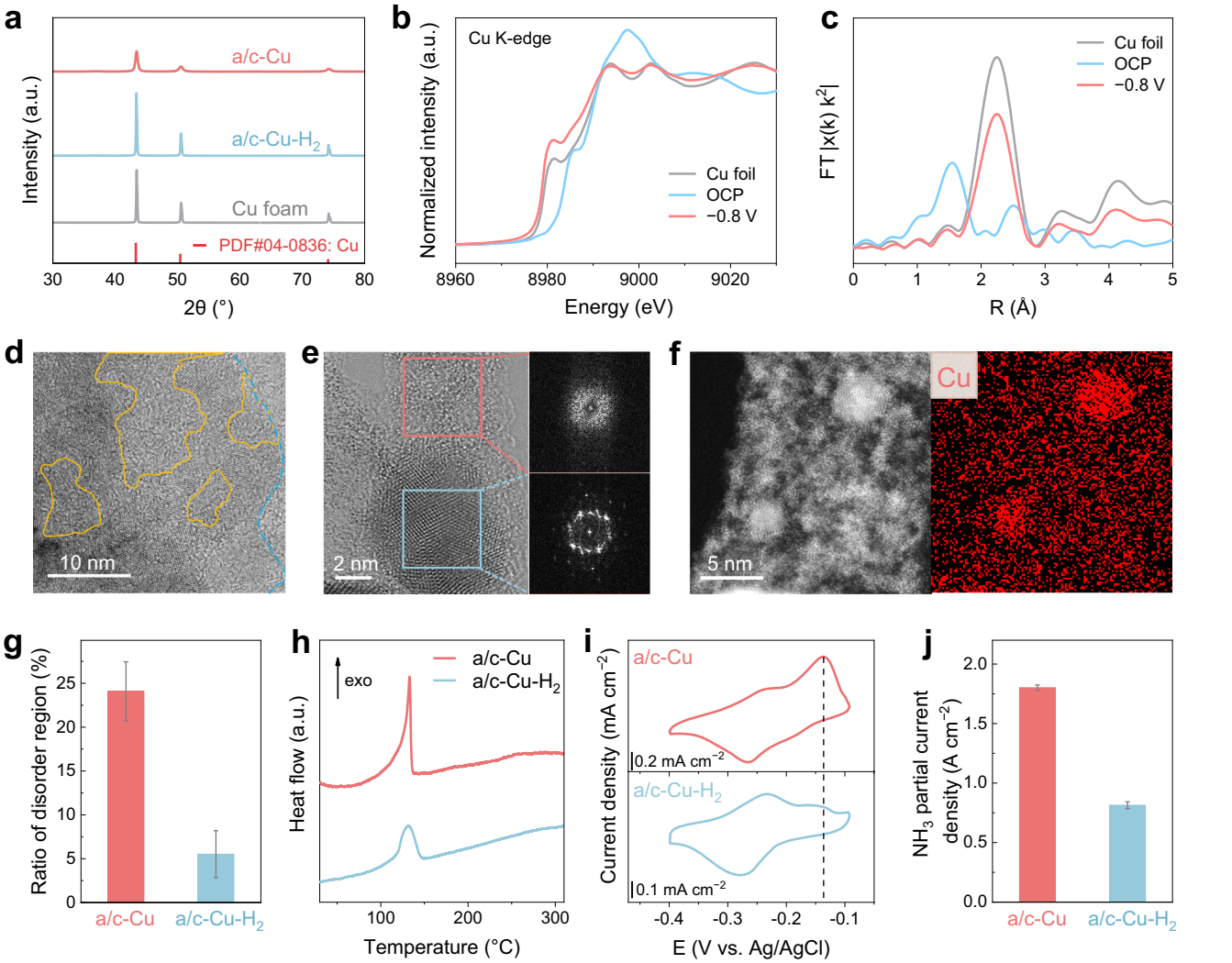

Fig. 2 | Structure characterizations. a XRD patterns of a/c-Cu and a/c-Cu-H_2 catalysts after NO_3^-RR. Operando **b** normalized XANES and **c** Fourier-transformed EXAFS spectra of a/c-Cu catalyst at a working potential of −0.8 V (vs. RHE). **d** HRTEM images of a/c-Cu catalyst and **e** corresponding FFT patterns acquired from different regions. **f** HAADF-STEM image and corresponding EDS element map of a/c-Cu catalyst. **g** Ratios of amorphous Cu domains. The error bars represent standard error of the mean and are made based on ten fully separate and identical measurements. **h** DSC curves. **i** CV curves of Pb stripping. **j** NH_3 partial current density at a cell voltage of 2.35 V over a/c-Cu and a/c-Cu-H_2 catalysts. The error bars represent standard error of the mean and are made based on three fully separate and identical measurements. Source data are provided as a Source Data file.

1.5 A cm^{-2} for over 50 h is further characterized by HAADF-STEM (Supplementary Figs. 31 and 32), and the amorphous Cu domains can be still observed, further indicating the good structural stability. Moreover, as evidenced by the electrochemical impedance spectra (EIS) in Supplementary Fig. 33, the poor conductivity of amorphous catalysts[45] has also been largely improved owing to the presence of adjacent crystalline Cu domains, resulting in low Ohmic resistance and thus low energy consumption for NH_3 production (Fig. 1c, f). Nevertheless, the stable amorphous/crystalline dual-phase structure of the a/c-Cu catalyst, is responsible for the high current density and long-term stability towards NH_3 synthesis.

Spectroscopic investigations

The NH_3 formation from NO_3^-RR involves multiple deoxygenation and hydrogenation steps which are closely associated with the adsorption of NO_3^- and N-containing intermediates as well as the generation of active hydrogen species from water dissociation[6,20]. To figure out how the dual-phase a/c-Cu catalyst promotes NO_3^-RR to NH_3, thorough spectroscopic characterizations and mechanistic investigation experiments were conducted (Supplementary Figs. 34 and 35). In situ Raman spectroscopy measurements were performed in a home-made flow cell to observe the adsorption and reduction of NO_3^- on the surface of the a/c-Cu catalyst. As shown in Fig. 3a, upon applying potentials, the NO_3^- species in the solution (1050 cm^{-1})[46] begin to adsorb onto catalyst surface, as evidenced by the characteristic Raman peaks at 1005 and 1370 cm^{-1} which correspond to the NO stretching vibration[47] and the NO_2 antisymmetric stretching vibration[48] of the adsorbed NO_3^- species, respectively. The Raman peak at 1098 cm^{-1}, assigned to copper-nitrate complexes, also suggests an interaction between copper and nitrate[47]. The Raman peaks at 1120 and 1259 cm^{-1} are typically assigned to the symmetric and antisymmetric stretching vibration of the important adsorbed NO_2^- intermediate in a nitro configuration[47,48]. Furthermore, the presence of the chelating nitrito configuration (*ONO*$^-$, at 1301 cm^{-1}) and the bridging nitro configuration (*N*OO^-, at 1435 cm^{-1}) further demonstrating the strong adsorption capacity for NO_x intermediates on the a/c-Cu catalyst[47,48]. The broad Raman peak at 1534 cm^{-1} is likely be assigned to the ν(N = O) of HNO* (1530 cm^{-1}) and the antisymmetric bending vibration of the HNH of NH_3 (1550 cm^{-1})[47,48]. However, when the applied potential becomes more negative, the intensities of NO_x peaks decrease significantly while

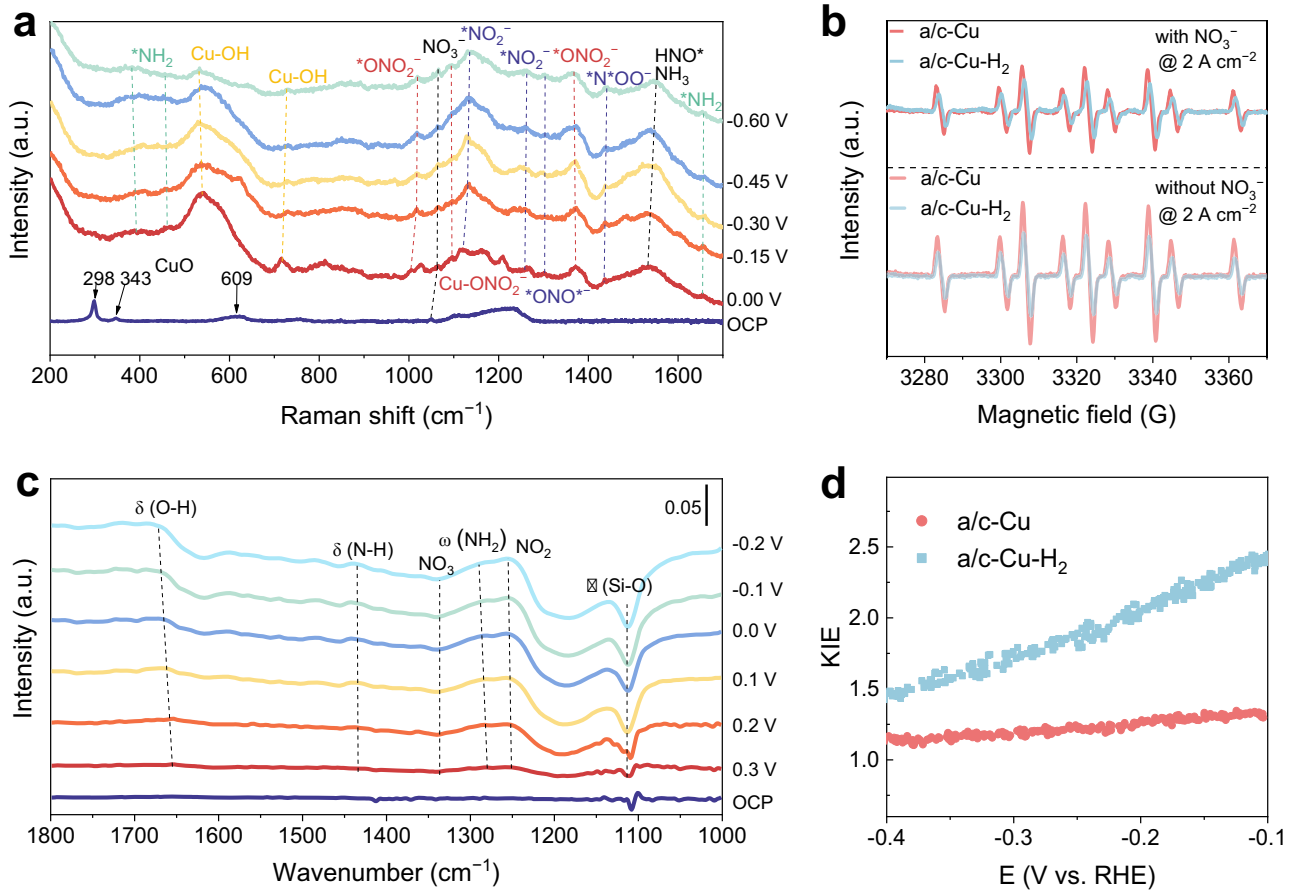

Fig. 3 | Spectroscopic investigations. a In situ Raman spectra over a/c-Cu catalyst at different potentials (vs. RHE). **b** EPR spectra of outlet electrolytes with or without KNO_3 using DMPO as radical trapping reagent. **c** In situ ATR-SEIRAS spectra over a/c-Cu catalyst at different potentials (vs. RHE) and **d** KIEs over a/c-Cu and a/c-Cu-H_2 catalysts. Source data are provided as a Source Data file.

that of the Cu-NH_2 (387 and 446 cm^{-1})[49] and the N–H bending mode of NH_2 (1654 cm^{-1})[50] increase, indicative of the fast conversion of NO_x species. On the other hand, these important intermediates are almost invisible over the a/c-Cu-H_2 catalyst (Supplementary Fig. 36). This is probably associated with the presence of the amorphous Cu domains with abundant low-coordinated sites that are considered to be active for NO_3^-RR[51,52]. The presence of the adsorbed species over the a/c-Cu catalyst was further validated by in situ attenuated total reflectance surface-enhanced infrared absorption spectroscopy (ATR-SEIRAS) measurements (Fig. 3c). The downward and upward IR bands at 1340 and 1256 cm^{-1} confirm the consumption and generation of NO_3^- and $*NO_2$, respectively[53]. At the same time, the N–H bending band at 1442 cm^{-1} and the NH_2 wagging band at 1294 cm^{-1} are also detected owing to NH_3 formation[54,55].

Apart from the adsorbed species, potential-dependent surface structure changes are also observed by in situ Raman measurements. The disappearance of the Raman peak at 298, 343, and 609 cm^{-1} assigned to CuO at open circuit potential (OCP) indicates the reduction of CuO to metallic Cu during NO_3^-RR (Fig. 3a), consistent with XRD, quasi in situ XPS, and XANES results. Meanwhile, the two emerging Raman peaks at 539 and 716 cm^{-1} can be assigned to the symmetric stretching of Cu–OH[56,57] and the bending mode of Cu–OH[58,59], respectively. The surface-adsorbed –OH is considered to be produced from water dissociation during NO_3^-RR (Fig. 3a). In contrast, only minor symmetric stretching of Cu–OH Raman peak can be observed over the a/c-Cu-H_2 catalyst (Supplementary Fig. 36), indicating the more favorable water dissociation owing to the presence of the amorphous Cu domains. The improved water disassociation is further verified by directly detecting the other dissociation product, adsorbed hydrogen (*H) species, at an applied current density of 2 A cm^{-2}. The *H detection was performed through being trapped with 5,5-dimethyl-1-pyrroline-N-oxide (DMPO) followed by electron paramagnetic resonance (EPR) measurements. Upon electrolysis in the absence of NO_3^- at 2 A cm^{-2}, the DMPO-H intensity of the a/c-Cu catalyst is much higher than that of the a/c-Cu-H_2, indicating the a/c-Cu has stronger ability to drive the H_2O dissociation and generate abundant *H species[60]. After adding NO_3^-, the DMPO-H intensity of both the a/c-Cu and a/c-Cu-H_2 catalyst decrease significantly due to the *H consumption by NO_3^- reduction. However, the stronger DMPO-H peaks over the a/c-Cu catalyst indicate the more favorable *H generation compared with the a/c-Cu-H_2 catalyst[61], in agreement with the Raman results. As hydrogenation steps are significantly affected by proton transfer rate, the kinetic isotope effect (KIE) of H/D is determined. When D_2O is used instead of H_2O in the electrolyte, the current density decreases (Supplementary Fig. 37). The KIE over the a/c-Cu catalyst is ~1.2, much lower than that over the a/c-Cu-H_2 catalyst (Fig. 3e), further highlighting the facilitated water disassociation[34].

Therefore, we have experimentally shown that the dual-phase a/c-Cu catalyst with rich amorphous Cu domains also plays dual roles in NO_3^-RR to NH_3, namely, improving the adsorption of N-containing intermediates and facilitating the formation of active hydrogen species from water dissociation.

Density functional theory (DFT) calculations

The dual roles of the amorphous Cu domains present in the a/c-Cu catalyst were further validated by DFT calculations. As Cu(100) was the

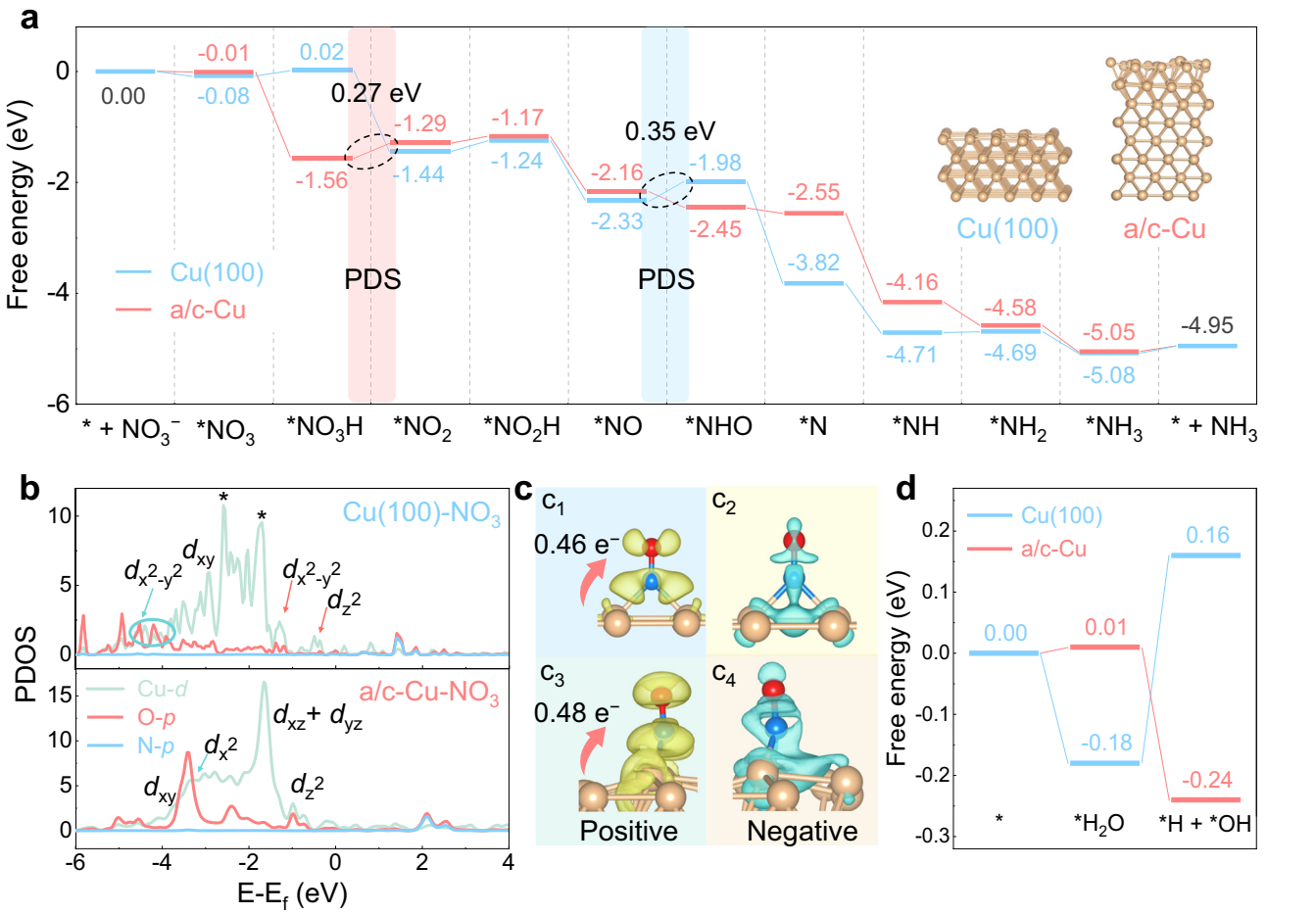

Fig. 4 | DFT calculations. a Reaction pathways of NO_3^-RR on Cu(100) and a/c-Cu. The inserts are atomic models for Cu(100) and a/c-Cu. **b** Projected density of states of $*NO_3$ adsorbed on Cu(100) and a/c-Cu. The asterisks represent the sum of other *d*-orbitals. **c** Charge density difference between *NO and Cu(100) (c_1 and c_2), *NO and a/c-Cu (c_3 and c_4). Isosurface = 2×10^{-3} e/Å^3. **d** Reaction pathway for water dissociation on Cu(100) and a/c-Cu. Source data are provided as a Source Data file.

main facet in the a/c-Cu catalyst (Supplementary Fig. 28), the amorphous/crystalline dual-phase Cu structure was modelled by ab initio molecular dynamics (AIMD) simulations using a slab with four Cu(100) layers, of which the top two layers were relaxed and the bottom two layers were fixed[62]. For the AIMD simulations, a temperature of 800 K was employed to accelerate structural sampling, facilitating the generation of an amorphous Cu surface. The free energy profiles of NO_3^-RR over Cu(100) and the amorphous phase of the a/c-Cu model were first studied, as shown in Fig. 4a and Supplementary Figs. 38 and 39. Firstly, $*NO_3$ adsorbs on the Cu(100) and a/c-Cu surfaces with energies of −0.08 and −0.01 eV, respectively. On the Cu(100) surface, the subsequent $*NO_3$ hydrogenation to $*NO_3H$ undergoes an uphill with an energy of 0.10 eV and the potential-determining step (PDS) is *NO hydrogenation to *NHO with an energy of 0.35 eV (Fig. 4a). In contrast, the a/c-Cu surface significantly improves $*NO_3$ hydrogenation with a distinct downhill trend. In this case, the PDS shifts to the formation of $*NO_2$ from $*NO_3H$ with a lower energy of 0.27 eV.

As the adsorption and activation of NO_3^- is the initial reaction step[63,64], we further estimated the projected density of states (PDOS) of $*NO_3$ (Fig. 4b). For $*NO_3$ adsorbed on Cu(100), the p_y orbital of O and the $d_{x2\text{-}y2}$ of Cu form a hybrid orbital in the range from −3.89 to −5.21 eV below the Fermi level (The detailed splitting *d*-orbitals of Cu and *p*-orbitals of O are displayed in Supplementary Fig. 40). For a/c-Cu, the p_x+p_y orbital of O and the $d_{x2\text{-}y2}$ + d_{xz} of Cu form a hybrid orbital in the range from −3.30 to −3.65 eV below the Fermi level (Supplementary Fig. 41). The hybridization region on a/c-Cu is closer to the Fermi level than that on Cu(100), which rationalizes the more favorable $*NO_3$ hydrogenation. The *NO hydrogenation process has been generally considered as the PDS in an alkaline environment[63,65,66], but in this work the PDS shifts from *NO hydrogenation on Cu(100) to the formation of $*NO_2$ on a/c-Cu. Thus, we estimated the charge density difference for the *NO intermediate. As shown in Fig. 4c, there is obvious charge transfer between *NO and Cu atoms on both Cu(100) (Fig. 4c_1, c_2) and a/c-Cu (Fig. 4c_3, c_4). However, the charge density is substantially discrete for *NO adsorbed on a/c-Cu. This is largely related to the disordered arrangement of the amorphous phase of a/c-Cu, which leads to drastic *d*-orbital electron splitting and facilitates electron transfer to *NO. Thus, the *NO hydrogenation to *NHO is remarkably improved and becomes an exothermic process on a/c-Cu.

The *H formation from water dissociation was further investigated on Cu(100) and a/c-Cu. As shown in Fig. 4d and Supplementary Fig. 42, the dissociation of H–OH on Cu(100) requires an energy input of 0.34 eV, much more difficult than the downhill process on a/c-Cu, consistent with the experimentally KIE results (Fig. 3e)[38]. Overall, the above theoretical investigations further demonstrate that the amorphous Cu structure present in the amorphous/crystalline dual-phase Cu catalyst promotes NO_3^-RR to NH_3 by optimizing the adsorption of N-containing intermediates and facilitating water dissociation.

Discussion

In summary, we have developed an a/c-Cu catalyst with stable amorphous/crystalline dual-phase structure, by annealing a commercially available Cu foam. The a/c-Cu catalyst exhibits impressive NO_3^-RR

performance in an alkaline MEA electrolyzer, with a NH_3 partial current density of 3.33 ± 0.005 A cm^{-2} and a NH_3 formation rate of 15.5 ± 0.02 mmol h^{-1} cm^{-2} at a low cell voltage of 2.6 ± 0.01 V. Moreover, the NH_3 Faradaic efficiency maintains around 90% at an applied current density of 1.5 A cm^{-2} for 300 h. The scale-up demonstration with an electrode size of 100 cm^2 achieves a maximum NH_3 formation rate up to 11.9 ± 0.5 g h^{-1} and an energy consumption of 108.3 ± 0.47 kJ g^{-1}_{NH3} at an applied current of 160 A. The high NH_3 formation rate is ascribed to the amorphous Cu domains present in the dual-phase a/c-Cu catalyst, which promote NO_3^-RR by optimizing the adsorption of N-containing intermediates and facilitating the formation of active hydrogen species from water dissociation. This work highlights the importance of stabilizing metastable amorphous structures for improving electrocatalytic reactivity and long-term stability.

Methods

Chemicals and materials

Cu foams (>99.9%) were purchased from Keshenghe Suzhou. Copper(II) chloride dihydrate ($CuCl_2{\cdot}2H_2O$, >99%) was purchased from Tianjin Kemiou Chemical Reagent Co., Ltd. Sodium hydroxide (NaOH, >96%), potassium nitrate (KNO_3, >99%), ammonium chloride (NH_4Cl, >99.8%), trisodium citrate dihydrate (>99%), phosphoric acid (H_3PO_4, >85%), hydrochloric acid (HCl, >36%) and ethylene glycol (>99%) were purchased from Sinopharm Chemical Reagent Co., Ltd. Potassium hydroxide (KOH, >95%), Nafion ionomer (5%), salicylic acid (>99.5%), sulfonamide (>99.8%), lead(II) perchlorate hydrate ($Pb(ClO_4)_2{\cdot}3H_2O$, >95%) and tannic acid (>99%) were purchased from Macklin. 5,5-dimethyl-1-pyrroline-N-oxide (DMPO, >97%) and potassium nitrite (KNO_2, >97%) were purchased from Aladdin. N-(1-naphthyl) ethylenediamine dihydrochloride (>98%) was purchased from Sigma-Aldrich (Shanghai) Trading Co., Ltd. Sodium nitroferricyanide ($C_5FeN_6Na_2O$, >99%) was purchased from Shanghai Chemical Reagent Co. Ir black catalyst was purchased from Johnson Matthey Corp. Ultrapure water (18.2 MΩ) was used in all experiments. All the chemicals were used without further purification.

Catalyst preparation

A commercial Cu foam with a geometric area of 1 cm^2 and a thickness of 0.2 mm (roughly 30 mg) was firstly annealed in air at 600 °C for 3 h. Subsequently, the annealed Cu foam was in situ electrochemically reduced during NO_3^-RR to form the a/c-Cu catalyst. The a/c-Cu-H_2 catalyst was prepared by treating the above air-annealed Cu foam in 5% H_2/Ar (50 mL min^{-1}) at 350 °C for 3 h. Control samples (a/c-Cu-300 and a/c-Cu-900) were also prepared with the same method, but the annealing temperatures were 300 and 900 °C, respectively. An amorphous Cu catalyst was prepared with a method from previous literature[67]. A homogenous solution was formed by dissolving 0.2 g of $CuCl_2{\cdot}2H_2O$ in 40 mL of ethylene glycol and stirring for 30 min. After adding 160 mg of tannic acid, the mixture was stirred for another 30 min. Then, 2 mL of 1.0 M NaOH was gradually added the above solution, followed by stirring for another 10 min. The amorphous Cu catalyst was washed three times with water and acetone, respectively, and then dried in vacuum overnight.

Materials characterizations

XRD patterns were obtained using a PANalytical X'pert PPR diffractometer equipped with a Cu Kα radiation source (λ = 1.5418 Å). SEM images were captured using a JSM-7900F Field-Emission SEM. HRTEM images were obtained using a JEM-2100 with an accelerating voltage of 200 kV. HAADF-STEM images were acquired with a JEM-ARM200F (JEOL, Japan). The ratio of amorphous domains was quantified from HRTEM images using Gatan Microscopy Suite (GMS-3) software and ImageJ software, and was defined as the total amorphous area divided by the overall catalyst area in each image. Error bars were made based on ten independent measurements.

Operando XAS measurements were carried out at the BL11B, BL14W1, and BL20U beamlines of the Shanghai Synchrotron Radiation Facility (SSRF). Energy calibration was performed using the absorption edge of a Cu foil as a reference. A home-made flow cell was used for XAS measurements in fluorescence mode (Supplementary Fig. 19), with a catalyst-coated gas diffusion electrode as working electrode. The anolyte and catholyte were 1 M KOH solution (5 mL min^{-1}) and 1 M KOH + 0.2 M KNO_3 solution (5 mL min^{-1}), respectively. The XAS data was analyzed using the ATHENA and ARTEMIS software.

In situ Raman spectroscopy measurements were carried out using a Renishaw inVia Raman microscope with a 785 nm near-infrared laser (Supplementary Fig. 34). The laser power was set to 1% and the exposure time was 50 s. A home-made flow cell with three electrodes was used for the Raman characterization. The cell was equipped with catalyst-coated gas diffusion electrode as the working electrode, a Pt wire as counter electrode, and an Ag/AgCl reference electrode. The cell had a quartz optical window, approximately 6 mm away from the working electrode, and the space in between was filled with catholyte. The anolyte and catholyte were 1 M KOH solution (5 mL min^{-1}) and 1 M KOH + 0.2 M KNO_3 solution (5 mL min^{-1}), respectively. The spectra were collected at different potentials after electrolysis for at least 2 min.

In situ ATR-SEIRAS measurement was conducted using an INVENIO S FTIR spectrometer with MCT detector (Supplementary Fig. 35). A home-made H cell was used for ATR-SEIRAS measurement, with Pt wire as a counter electrode and Ag/AgCl electrode as a reference electrode. For working electrode, an Au film was sputtered onto a silicon prism, followed by drop-casting a catalyst ink onto the Au film. All spectra were presented as relative change in absorbance, referenced to background spectra collected at OCP.

Quasi in situ XPS and Auger electron spectroscopy (AES) measurements were conducted using a Thermo Scientific ESCALAB 250Xi spectrometer with an Al Kα X-ray source. The NO_3^-RR measurements were carried out in a MEA electrolyzer inside a glovebox, maintaining an O_2 concentration below 0.01 ppm. After electrolysis for at least 20 min, the electrodes were transferred into the XPS analysis chamber using a mobile transfer chamber, without air exposure during the transfer process.

EPR spectroscopy measurements were conducted using a Bruker A200 spectrometer. A DMPO solution (10 mg mL^{-1}) as a radical trapping reagent was added to the catholyte. After NO_3^-RR in a MEA electrolyzer, the catholyte was collected, rapidly frozen in liquid nitrogen to prevent degradation, and then thawed for EPR analysis.

DSC measurements was carried out using NETZSCH DSC300 Select with a heat rate of 5 °C min^{-1} under N_2 atmosphere. Both the a/c-Cu and a/c-Cu-H_2 powder catalysts were used for measurements.

The hydroxide (OH^-) electrosorption experiments were performed through cyclic voltammetry (CV) measurements in an H-cell, using Ar-saturated 1 M KOH aqueous solution. The potential window was set from −0.8 to −0.523 V vs. Ag/AgCl, with a scan rate of 10 mV s^{-1}. Before CV measurements, the electrode was firstly pre-reduced under NO_3^-RR conditions by applying a potential of −2.0 V vs. Ag/AgCl for 15 min.

The Pb UPD measurements for characterizing low-coordinated Cu sites were referred to in the literature[41]. Following NO_3^-RR at an applied potential of −2.0 V vs. Ag/AgCl for 15 min, the catalysts were measured by CV in a solution containing 0.1 M $NaClO_4$, 10 mM $HClO_4$, and 3 mM $Pb(ClO_4)_2$. The potential range was set from −0.4 to −0.1 V vs. Ag/AgCl, with a scan rate of 10 mV s^{-1}. The characteristic peak at −0.15 V vs. Ag/AgCl was identified as low-coordinated Cu sites.

The H/D KIE experiments were conducted using the linear sweep voltammetry (LSV) in H-cell at a scan rate of 10 mV s^{-1}, with iR correction. The electrode was firstly pre-reduced under NO_3^-RR conditions at an applied potential of −2.0 V vs. Ag/AgCl for 15 min. Subsequently, LSV measurements was carried out in the electrolyte, which consisted

of 0.2 M KNO_3 and 1.0 M KOH, with either H_2O or D_2O as the solvent. The KIE values were calculated based on the ratio of current density measured in H_2O to that measured in D_2O.

NO_3^-RR measurements

NO_3^-RR performance was assessed using an alkaline MEA electrolyzer at ambient temperature (20–25 °C)[68]. The electrolyzer was assembled using a graphite flow field plate for catholyte and Pt-coated titanium flow field plates for anolyte (Supplementary Fig. 2). A quaternary ammonia poly(N-methyl-piperidine-co-p-terphenyl) (QAPPT) membrane was used as an anion exchange membrane. The anode was prepared by coating an ink of QAPPT-impregnated Ir black catalyst (1.5 mg cm^{-2}) onto a porous foam. The annealed Cu foam with a geometric area of 1 cm^2 was directly used as an integrated porous electrode, if not stated otherwise. For comparison, the annealed foam was also ground into powder and drop-casted onto a carbon paper to form a conventional gas diffusion electrode. The NO_3^-RR measurements were performed in the galvanostatic mode using an Ivium electrochemical workstation. The anolyte and catholyte were 1 M KOH solution (5 mL min^{-1}) and 1 M KOH + 0.2 M KNO_3 solution (3 mL min^{-1}), respectively. In the scale-up experiments, an annealed Cu foam with a geometric area of 100 cm^2 was used and the catholyte was 1 M KOH + 0.5 M KNO_3 (50 mL min^{-1}). In all the performance measurements including 300-h stability test, all the electrolytes were not recirculated and fresh electrolytes were always used. The NO_3^-RR measurements were performed in the galvanostatic mode using a Keysight N8940A autoranging system direct current (DC) power supply (0–80 V/0–170 A, 5000 W). The electrolysis durations at each applied current were 15 and 10 min for 1-cm^2 and 100-cm^2 electrolyzers, respectively. Both catholyte and anolyte were collected at each applied current for subsequent liquid product analysis.

Products analysis

Gas products (i.e., H_2 in this work) were quantified using an on-line gas chromatography (Agilent, GC 8860), equipped with a thermal conductivity detector (TCD). Liquid products (NO_2^- and NH_3) were analyzed by UV–vis spectrophotometer (Shimadzu, Uv–2700i).

For NH_3 quantification, the indophenol blue method was conducted. Specifically, 2 mL of 1 M NaOH solution containing 5.0 wt% salicylic acid and 5.0 wt% sodium citrate, followed by 1 mL of 0.05 M NaClO, and 0.2 mL of 1 wt% $C_5FeN_6Na_2O$ (sodium nitroferricyanide), were successively introduced into 2 mL of the diluted electrolyte, kept in the dark for 2 h. The NH_3 concentration was determined based on the absorbance at 655 nm. Additionally, ^{1}H-NMR spectroscopy was also used to quantify the NH_3 (NH_4^+) production using a JEOL JNM-ECZL400S NMR spectrometer. In a typical procedure, 0.5 mL of standard solution/electrolyte was adjusted to pH 2 by adding 0.6 mL of 1.0 M HCl. Next, 0.5 mL of the above solution was mixed with the 0.1 mL DMSO-*d6* (containing 2.5 mg mL^{-1} $C_4H_4O_4$ as an internal standard). The quantification of NH_4^+ was calculated with the peak area ratio of NH_4^+ versus $C_4H_4O_4$.

For NO_2^- quantification, the Griess method was employed. Specifically, after neutralizing 3 mL of the diluted electrolyte with 3 mL of 1.0 M HCl, 0.1 mL of Griess color reagent, containing 4 g of sulfonamide, 10 mL of H_3PO_4 (85%), and 0.2 g of N-(1-naphthyl) ethylenediamine dihydrochloride in 100 mL of water, was added. The mixture was then kept in the dark for 20 min. The NO_2^- concentration was determined based on the absorbance at 540 nm.

The Faradaic efficiency of product i is calculated as follows:

$$\varepsilon_{Faradaic,\,i} = Q_i/Q_{total} \times 100 = (N_i \times n_i \times F)/Q_{total} \times 100 \quad (1)$$

Where, $\varepsilon_{Faradaic,i}$: the Faradaic efficiency of product i, Q_{total}: the consumed charge, C; N_i: the amount of the product i, mol; n_i: the number of transferred charge in the product i; F: Faraday constant, 96485 C mol^{-1}.

The NH_3 partial current density is calculated as follows:

$$j_{NH3} = j_{total} \times \varepsilon_{Faradaic,\,NH3} \quad (2)$$

The full-cell energy efficiency (EE) of NH_3 is defined as follows:

$$EE_{NH3} = (1.23 - E^0{}_{NH3}) \times \varepsilon_{Faradaic,\,NH3}/U \quad (3)$$

Where, EE_{NH3}: the full-cell energy efficiency (EE) of NH_3, %; 1.23: the equilibrium potential of oxygen evolution reaction, V vs. RHE; E^0_{NH3}: the equilibrium potential of NO_3^- to NH_3, which is 0.69 V vs. RHE[19]; U: cell voltage, V.

The energy consumption for NH_3 production is defined as follows[33]:

$$\text{Energy consumption} = I \times U/(C_{NH3} \times v \times 17) \quad (4)$$

Where, energy consumption: kJ g^{-1}_{NH3}; I: the applied current, A; C_{NH3}: the molar concentration of NH_3, mol L^{-1}; v: the flow rate of the catholyte, L s^{-1}; 17: the molecular mass of NH_3, g mol^{-1}.

Computational details

All simulations were carried out using the Vienna ab initio simulation package (VASP 6.2.0)[69]. Electron-ion interactions were described by the projector-augmented wave (PAW) pseudopotentials with a cutoff energy of 450 eV[70]. For electron exchange and correlation energies, the Perdew–Burke–Ernzerh of generalized gradient approximation (GGA-PBE) was represented[71]. DFT-D3 with Becke–Jonson (BJ) damping method was used to correct the long-range van der Waals interaction[72]. The exchange-correlation functional with a Gaussian smearing width term of 0.05 eV was used. The convergence criteria for force and electronic self-consistent iteration were set to 0.01 eV $Å^{-1}$ and 1×10^{-5} eV, respectively. In addition, all calculations are spin-polarized. For all surface optimization, the sampling of the Brillouin zone was performed using a Monkhorst–Pack scheme of (2 × 2 × 1). For all DOS calculation, the sampling of the Brillouin zone was performed using a Monkhorst–Pack scheme of (5 × 5 × 1)[73]. The vacuum layer of 15 Å were selected to prevent their periodic images between adjacent layers. The VASPKIT code was used for postprocessing computational data obtained from VASP[74].

For the adsorption of $*NO_3$, the energy of HNO_3 in the liquid phase is converted to $*NO_3$ proton by the change of entropy as a correction factor, as shown below:

The adsorption energy of NO_3^- (ΔG^*_{NO3}) is approximately expressed as:

$$\Delta G_{*NO3} = G_{*NO3} - G_* - G_{HNO3} + 0.5G_{H2} + \Delta G_{correct} \quad (5)$$

$$\Delta G_{correct} = -\Delta G_{S1} - \Delta G_{S2} \quad (6)$$

where G_{*NO3}, G_*, G_{HNO3}, and G_{H2} are the Gibbs free energy of NO_3 adsorbed on Cu substrates, Cu substrates, HNO_3, and H_2 molecules in the gas phase, respectively. According to CRC handbook of chemistry and physics[75], $\Delta G_{S1} = -0.075$ eV and $\Delta G_{S2} = -0.317$ eV. Therefore, $\Delta G_{correct}$ is set to 0.075 + 0.317 = 0.392 eV.

The Cu(100) model was constructed using a 4 × 4 × 1 supercell comprising four layers and a total of 112 Cu atoms. For the a/c-Cu model, a slab with four Cu(100) layers was generated, with the bottom two layers fixed and the top two layers relaxed during AIMD simulations[62]. A time step of 2 fs was used, initially under constant-pressure conditions as the temperature was ramped from 300 K to 800 K. Subsequently, a canonical ensemble (NVT) was employed with a

Nose–Hoover thermostat set at 800 K to accelerate structural sampling and facilitate the formation of an amorphous Cu surface. The first 15 ps of AIMD served as the equilibration period, followed by a 5 ps production run for data collection and analysis.

Data availability

The data that support the findings of this study are available within the paper and the Supplementary Information. Other relevant data are available from the corresponding authors on reasonable request. Source data are provided with this paper.

References

1. Chen, J. G. et al. Beyond fossil fuel-driven nitrogen transformations. *Science* **360**, eaar6611 (2018).
2. Suryanto, B. H. et al. Challenges and prospects in the catalysis of electroreduction of nitrogen to ammonia. *Nat. Catal.* **2**, 290–296 (2019).
3. van Langevelde, P. H., Katsounaros, I. & Koper, M. T. Electrocatalytic nitrate reduction for sustainable ammonia production. *Joule* **5**, 290–294 (2021).
4. Xu, H., Ma, Y., Chen, J., Zhang, W. X. & Yang, J. Electrocatalytic reduction of nitrate - a step towards a sustainable nitrogen cycle. *Chem. Soc. Rev.* **51**, 2710–2758 (2022).
5. Li, P. et al. Pulsed nitrate-to-ammonia electroreduction facilitated by tandem catalysis of nitrite intermediates. *J. Am. Chem. Soc.* **145**, 6471–6479 (2023).
6. Li, J. et al. Efficient ammonia electrosynthesis from nitrate on strained ruthenium nanoclusters. *J. Am. Chem. Soc.* **142**, 7036–7046 (2020).
7. Fan, K. et al. Active hydrogen boosts electrochemical nitrate reduction to ammonia. *Nat. Commun.* **13**, 7958 (2022).
8. He, W. et al. Splicing the active phases of copper/cobalt-based catalysts achieves high-rate tandem electroreduction of nitrate to ammonia. *Nat. Commun.* **13**, 1129 (2022).
9. Chen, F. Y. et al. Efficient conversion of low-concentration nitrate sources into ammonia on a Ru-dispersed Cu nanowire electrocatalyst. *Nat. Nanotechnol.* **17**, 759–767 (2022).
10. Lim, J. et al. Structure sensitivity of Pd facets for enhanced electrochemical nitrate reduction to ammonia. *ACS Catal.* **11**, 7568–7577 (2021).
11. Yang, J., Sebastian, P., Duca, M., Hoogenboom, T. & Koper, M. T. pH dependence of the electroreduction of nitrate on Rh and Pt polycrystalline electrodes. *Chem. Commun.* **50**, 2148–2151 (2014).
12. Zhou, J. et al. Regulating active hydrogen adsorbed on grain boundary defects of nano-nickel for boosting ammonia electrosynthesis from nitrate. *Energy Environ. Sci.* **16**, 2611–2620 (2023).
13. Wang, Y., Zhou, W., Jia, R., Yu, Y. & Zhang, B. Unveiling the activity origin of a copper-based electrocatalyst for selective nitrate reduction to ammonia. *Angew. Chem. Int. Ed.* **59**, 5350–5354 (2020).
14. Daiyan, R. et al. Nitrate reduction to ammonium: from CuO defect engineering to waste NO_x-to-NH_3 economic feasibility. *Energy Environ. Sci.* **14**, 3588–3598 (2021).
15. Zhang, G. et al. Tandem electrocatalytic nitrate reduction to ammonia on MBenes. *Angew. Chem. Int. Ed.* **62**, e202300054 (2023).
16. Duan, W. et al. In situ reconstruction of metal oxide cathodes for ammonium generation from high-strength nitrate wastewater: Elucidating the role of the substrate in the performance of Co_3O_{4-x}. *Environ. Sci. Technol.* **57**, 3893–3904 (2023).
17. Wu, Z. Y. et al. Electrochemical ammonia synthesis via nitrate reduction on Fe single atom catalyst. *Nat. Commun.* **12**, 2870 (2021).
18. Deng, X., Yang, Y., Wang, L., Fu, X. Z. & Luo, J. L. Metallic Co nanoarray catalyzes selective NH_3 production from electrochemical nitrate reduction at current densities exceeding 2 A cm^{-2}. *Adv. Sci.* **8**, 2004523 (2021).
19. Wang, Y. et al. Enhanced nitrate-to-ammonia activity on copper-nickel alloys via tuning of intermediate adsorption. *J. Am. Chem. Soc.* **142**, 5702–5708 (2020).
20. Fang, J. Y. et al. Ampere-level current density ammonia electrochemical synthesis using CuCo nanosheets simulating nitrite reductase bifunctional nature. *Nat. Commun.* **13**, 7899 (2022).
21. Liang, S., Teng, X., Xu, H., Chen, L. & Shi, J. H. Species regulation by Mn-$Co(OH)_2$ for efficient nitrate electro-reduction in neutral solution. *Angew. Chem. Int. Ed.* **63**, e202400206 (2024).
22. Gao, Q. et al. Breaking adsorption-energy scaling limitations of electrocatalytic nitrate reduction on intermetallic CuPd nanocubes by machine-learned insights. *Nat. Commun.* **13**, 2338 (2022).
23. Shahid, U. B., Kwon, Y., Yuan, Y., Gu, S. & Shao, M. High-performance ammonia electrosynthesis from nitrate in a NaOH-KOH-H_2O ternary electrolyte. *Angew. Chem. Int. Ed.* **63**, e202403633 (2024).
24. Reyter, D., Bélanger, D. & Roué, L. Study of the electroreduction of nitrate on copper in alkaline solution. *Electrochim. Acta* **53**, 5977–5984 (2008).
25. Wang, W., Chen, J. & Tse, E. C. Synergy between Cu and Co in a layered double hydroxide enables close to 100% nitrate-to-ammonia selectivity. *J. Am. Chem. Soc.* **145**, 26678–26687 (2023).
26. Pei, Y. et al. Synthesis and catalysis of chemically reduced metal-metalloid amorphous alloys. *Chem. Soc. Rev.* **41**, 8140–8162 (2012).
27. Chen, C. et al. Oxidation of metallic Cu by supercritical CO_2 and control synthesis of amorphous nano-metal catalysts for CO_2 electroreduction. *Nat. Commun.* **14**, 1092 (2023).
28. Bauers, S. R. et al. Structural evolution of iron antimonides from amorphous precursors to crystalline products studied by total scattering techniques. *J. Am. Chem. Soc.* **137**, 9652–9658 (2015).
29. Shen, Z. et al. Highly distributed amorphous copper catalyst for efficient ammonia electrosynthesis from nitrate. *J. Hazard. Mater.* **445**, 130651 (2023).
30. Zhai, Y. et al. Phase engineering of metal nanocatalysts for electrochemical CO_2 reduction. *eScience* **2**, 467–485 (2022).
31. Yang, Y. et al. Hierarchical nanoassembly of MoS_2/Co_9S_8/Ni_3S_2/Ni as a highly efficient electrocatalyst for overall water splitting in a wide pH range. *J. Am. Chem. Soc.* **141**, 10417–10430 (2019).
32. Zheng, W., Liu, M. & Lee, L. Y. S. Best practices in using foam-type electrodes for electrocatalytic performance benchmark. *ACS Energy Lett.* **5**, 3260–3264 (2020).
33. Xu, Z. et al. Continuous ammonia electrosynthesis using physically interlocked bipolar membrane at 1000 mA cm^{-2}. *Nat. Commun.* **14**, 1619 (2023).
34. Hu, Q. et al. Ammonia electrosynthesis from nitrate using a ruthenium-copper cocatalyst system: a full concentration range study. *J. Am. Chem. Soc.* **146**, 668–676 (2023).
35. Gan, L. et al. Redirecting surface reconstruction of CoP-Cu heterojunction to promote ammonia synthesis at industrial-level current density. *Chem. Eng. J.* **487**, 150429 (2024).
36. Guo, X. et al. Highly stable perovskite oxides for electrocatalytic acidic NO_x^- reduction streamlining ammonia synthesis from air. *Angew. Chem. Int. Ed.* **63**, e202410517 (2024).
37. Zhang, J. et al. Steering CO_2 electroreduction pathway toward ethanol via surface-bounded hydroxyl species-induced noncovalent interaction. *Proc. Natl Acad. Sci. USA* **120**, e2218987120 (2023).
38. Zhang, B. et al. Defect-induced triple synergistic modulation in copper for superior electrochemical ammonia production across broad nitrate concentrations. *Nat. Commun.* **15**, 2816 (2024).
39. Sang, J. et al. A Reconstructed $Cu_2P_2O_7$ catalyst for selective CO_2 electroreduction to multicarbon products. *Angew. Chem. Int. Ed.* **61**, e202114238 (2022).
40. Sheng, H. W., Wilde, G. & Ma, E. The competing crystalline and amorphous solid solutions in the Ag-Cu system. *Acta Mater.* **50**, 475–488 (2002).

41. Yang, Y. et al. Operando studies reveal active Cu nanograins for CO_2 electroreduction. *Nature* **614**, 262–269 (2023).
42. Zhou, Y. et al. Electronegativity-induced charge balancing to boost stability and activity of amorphous electrocatalysts. *Adv. Mater.* **34**, 2100537 (2022).
43. Jeon, S. et al. Reversible disorder-order transitions in atomic crystal nucleation. *Science* **371**, 498–503 (2021).
44. Loh, N. D. et al. Multistep nucleation of nanocrystals in aqueous solution. *Nat. Chem.* **9**, 77–82 (2016).
45. Jia, B. et al. Construction of amorphous/crystalline heterointerfaces for enhanced electrochemical processes. *eScience* **3**, 100112 (2023).
46. Zhou, Z., Huang, G. G., Kato, T. & Ozaki, Y. Experimental parameters for the SERS of nitrate ion for label-free semi-quantitative detection of proteins and mechanism for proteins to form SERS hot sites: a SERS study. *J. Raman Spectrosc.* **42**, 1713–1721 (2021).
47. Bai, L. et al. Electrocatalytic nitrate and nitrite reduction toward ammonia using Cu_2O nanocubes: active species and reaction mechanisms. *J. Am. Chem. Soc.* **146**, 9665–9678 (2024).
48. Butcher, D. P. Jr & Gewirth, A. A. Nitrate reduction pathways on Cu single crystal surfaces: Effect of oxide and Cl^-. *Nano Energy* **29**, 457–465 (2016).
49. Wang, Y. et al. Wide-pH-range adaptable ammonia electrosynthesis from nitrate on Cu-Pd interfaces. *Sci. China Chem.* **66**, 913–922 (2023).
50. Torreggiani, A., Esposti, A. D., Tamba, M., Marconi, G. & Fini, G. Experimental and theoretical Raman investigation on interactions of Cu(II) with histamine. *J. Raman Spectrosc.* **37**, 291–298 (2006).
51. Hu, Q. et al. Reaction intermediate-mediated electrocatalyst synthesis favors specified facet and defect exposure for efficient nitrate-ammonia conversion. *Energy Environ. Sci.* **14**, 4989–4997 (2021).
52. Huang, K. et al. Boosting nitrate to ammonia via the optimization of key intermediate processes by low-coordinated Cu–Cu Sites. *Adv. Funct. Mater.* **34**, 2315324 (2024).
53. Pérez-Gallent, E., Figueiredo, M. C., Katsounaros, I. & Koper, M. T. Electrocatalytic reduction of nitrate on copper single crystals in acidic and alkaline solutions. *Electrochim. Acta* **227**, 77–84 (2017).
54. Yao, Y., Zhu, S., Wang, H., Li, H. & Shao, M. A spectroscopic study of electrochemical nitrogen and nitrate reduction on rhodium surfaces. *Angew. Chem. Int. Ed.* **59**, 10479–10483 (2020).
55. Xu, M. et al. Kinetically matched C–N coupling toward efficient urea electrosynthesis enabled on copper single-atom alloy. *Nat. Commun.* **14**, 6994 (2023).
56. Shao, F. et al. Surface water as an initial proton source for the electrochemical CO reduction reaction on copper surfaces. *Angew. Chem. Int. Ed.* **62**, e202214210 (2022).
57. Jiao, J. et al. Steering the reaction pathway of CO_2 electroreduction by tuning the coordination mumber of copper catalysts. *J. Am. Chem. Soc.* **146**, 15917–15925 (2024).
58. Wei, D. et al. Surface adsorbed hydroxyl: a double-edged sword in electrochemical CO_2 reduction over oxide-derived copper. *Angew. Chem. Int. Ed.* **62**, e202306876 (2023).
59. Zhang, T. et al. Selective increase in CO_2 electroreduction to ethanol activity at nanograin-boundary-rich mixed Cu(I)/Cu(0) sites via enriching co-adsorbed CO and hydroxyl species *Angew. Chem. Int. Ed.* **63**, e202407748 (2024).
60. Li, X., Shen, P., Li, X., Ma, D. & Chu, K. Sub-nm RuO_x clusters on Pd metallene for synergistically enhanced nitrate electroreduction to ammonia. *ACS Nano* **17**, 1081–1090 (2023).
61. Wang, Y. et al. Phase-regulated active hydrogen behavior on molybdenum disulfide for electrochemical nitrate-to-ammonia conversion. *Angew. Chem. Int. Ed.* **63**, e202315109 (2024).
62. Joutsuka, T. & Tada, S. Adsorption of CO_2 on amorphous and crystalline zirconia: a DFT and experimental study. *J. Phys. Chem. C.* **127**, 6998–7008 (2023).
63. Wang, S. et al. Non-noble single-atom alloy for electrocatalytic nitrate reduction using hierarchical high-throughput screening. *Nano Energy* **113**, 108543 (2023).
64. Wang, S., Wang, Y., Fu, Y., Liu, T. & Wang, G. High-throughput mechanistic study of highly selective hydrogen-bonded organic frameworks for electrochemical nitrate reduction to ammonia. *J. Energy Chem.* **87**, 408–415 (2023).
65. Hu, T., Wang, C., Wang, M., Li, C. M. & Guo, C. Theoretical insights into superior nitrate reduction to ammonia performance of copper catalysts. *ACS Catal.* **11**, 14417–14427 (2021).
66. Shu, Z. et al. High-throughput screening of heterogeneous transition metal dual-atom catalysts by synergistic effect for nitrate reduction to ammonia. *Adv. Funct. Mater.* **33**, 2301493 (2023).
67. Yang, P.-P. et al. Highly enhanced chloride adsorption mediates efficient neutral CO_2 electroreduction over a dual-phase copper catalyst. *J. Am. Chem. Soc.* **145**, 8714–8725 (2024).
68. Wei, P. et al. Coverage-driven selectivity switch from ethylene to acetate in high-rate CO_2/CO electrolysis. *Nat. Nanotechnol.* **18**, 299–306 (2023).
69. Kresse, G. & Furthmüller, J. Efficient iterative schemes for ab initio total-energy calculations using a plane-wave basis set. *Phys. Rev. B* **54**, 11169–11186 (1996).
70. Blöchl, P. E. Projector augmented-wave method. *Phys. Rev. B* **50**, 17953–17979 (1994).
71. Perdew, J. P., Burke, K. & Ernzerhof, M. Generalized gradient approximation made simple. *Phys. Rev. Lett.* **78**, 1396–1396 (1997).
72. Grimme, S., Ehrlich, S. & Goerigk, L. Effect of the damping function in dispersion corrected density functional theory. *J. Comput. Chem.* **32**, 1456–1465 (2011).
73. Pack, J. D. & Monkhorst, H. J. "Special points for Brillouin-zone integrations"—a reply. *Phys. Rev. B* **16**, 1748–1749 (1977).
74. Yang, J. et al. Dynamic behavior of single-atom catalysts in electrocatalysis: Identification of Cu-N_3 as an active site for the oxygen reduction reaction. *J. Am. Chem. Soc.* **143**, 14530–14539 (2021).
75. Weast, R. C. *CRC Handbook of Chemistry and Physics*, 71st edn. (CRC Press, 1988).

Acknowledgements

This work was supported by the National Key R&D Program of China (2023YFA1508000, G.W.), the National Natural Science Foundation of China (22372171, D.G.; 22125205, G.W.; 22321002, G.W.; 22494711, D.G.), the Fundamental Research Funds for the Central Universities (20720220008, G.W.), the Strategic Priority Research Program of the Chinese Academy of Sciences (XDB0600200, G.W.), the Liaoning Revitalization Talents Program (XLYC2203178, D.G.), the Liaoning Binhai Laboratory (LBLF-2023-02, G.W.; LBLD-2024-02, D.G.), the Dalian Outstanding Young Scientist Foundation (2024RJ003, D.G.), the Dalian Institute of Chemical Physics (DICP I202203, D.G.), the Joint Fund of the Yulin University and the Dalian National Laboratory for Clean Energy (YLU-DNL Fund 2022008, G.W.), the China Postdoctoral Science Foundation (2023M743428, S.W.; GZC20232594, S.W.), the Yanchang Petroleum Group (yc-hw-2023ky-08, D.G.), and the Photon Science Center for Carbon Neutrality (JZHKYPT-2021-07, D.G.). We thank Prof. Jin-Xun Liu at the USTC and Prof. Zhangquan Peng, Dr. Zhiwei Zhao and Dr. Long Pang at the DICP for fruitful discussions. We also thank the staff at the BL11B, BL14W1, and BL20U beamlines of the SSRF for their technical assistance during XAS measurements.

Author contributions

Conceptualization: G.W. and D.G.; methodology: Y.W., S.W., Y.F., J.S., P.W., R.L., and D.G.; investigation: Y.W. and S.W.; visualization: Y.W., S.W., and D.G.; funding acquisition: G.W., D.G., and S.W.; supervision: G.W. and D.G.; writing—original draft: Y.W., S.W., and D.G.; writing—review and editing: D.G., G.W., and X.B.

Competing interests
The authors declare no competing interests.

Additional information
Supplementary information The online version contains supplementary material available at https://doi.org/10.1038/s41467-025-55889-9.

Correspondence and requests for materials should be addressed to Dunfeng Gao or Guoxiong Wang.

Peer review information *Nature Communications* thanks Dong-Hee Lim and the other, anonymous, reviewers for their contribution to the peer review of this work. A peer review file is available.